

Depth-of-focus extension in optical coherence tomography via multiple aperture synthesis

EN BO,¹ YUEMEI LUO,¹ SI CHEN,¹ XINYU LIU,¹ NANSHUO WANG,¹ XIN GE,¹ XIANGHONG WANG,¹ SHUFEN CHEN,¹ SHI CHEN,¹ JINHAN LI,¹ AND LINBO LIU^{1,2,*}

¹School of Electrical and Electronic Engineering, Nanyang Technological University, Singapore 639798, Singapore

²School of Chemical and Biomedical Engineering, Nanyang Technological University, Singapore 637459, Singapore

*Corresponding author: liulinbo@ntu.edu.sg

Received 13 March 2017; revised 10 May 2017; accepted 12 May 2017 (Doc. ID 290555); published 22 June 2017

In this paper, we report what we believe is a novel technique to overcome the depth-of-focus (DOF) limitation in optical coherence tomography (OCT). Using confocal optics on a sample arm, we scanned the illumination beam across the under-filled objective lens pupil plane by steering the beam at the pinhole using a microcylindrical lens. The detected interferometric signals from multiple distinctive apertures were digitally refocused, which is analogous to synthetic aperture radar (SAR). Using numerical simulations and imaging experiments, we verified that this technique can maintain a diffraction-limited transverse resolution along a DOF that is ~ 10 times larger than the confocal parameter. The ability to extend the DOF without signal loss and sidelobe artifacts may ultimately overcome the DOF limitation in high-resolution OCT. © 2017 Optical Society of America

OCIS codes: (110.4500) Optical coherence tomography; (170.4500) Optical coherence tomography; (120.3890) Medical optics instrumentation; (110.4850) Optical transfer functions.

<https://doi.org/10.1364/OPTICA.4.000701>

1. INTRODUCTION

Optical coherence tomography (OCT) is a cross-sectional, three-dimensional (3D) imaging technique that provides non-invasive, high-speed, high-resolution images of scattering media, such as inhomogeneous biological tissues [1]. Until now, this technique has been widely applied in ophthalmology [2] and cardiology [3]. In OCT, the transverse resolution Δx is determined by the diffraction-limited spot size of the sample focused beam and defined as the beam waist diameter under the assumption of a Gaussian input beam. This parameter can be expressed as $\Delta x = 2\lambda/\pi\text{NA}$, where $\text{NA} = d/2f$ is the numerical aperture (NA) of the objective lens. The corresponding depth of focus (DOF) can be defined as the confocal parameter and is expressed as $\text{DOF} = 4\lambda/\pi\text{NA}^2$, which represents the axial distance between the values of z (axial depth) where the size at the $1/e^2$ beam is two times larger than that at the beam waist. According to the definitions stated above, the transverse resolution is inversely proportional to the NA of the objective lens, and the DOF is proportional to the square of the transverse resolution. Consequently, a tradeoff occurs between the transverse resolution and the DOF in which a lower transverse resolution results in a larger DOF and vice versa.

To achieve high transverse resolution over an extended DOF, various approaches have been proposed. Axicon lenses and phase and amplitude pupil filters can generate a focus with Bessel beam characteristics, including a more uniform main lobe diameter in the transverse direction over an extended DOF compared with the confocal parameter [4,5]. However, in the spatial frequency

domain, Bessel beams suffer a major loss of spatial frequency components in the coherence transfer function (CTF) compared to that of Gaussian beams, which results in a significant decline of sensitivity and sidelobe artifacts in the OCT images [6]. Although these problems can be mitigated by dark-field Gaussian detection, the fundamental problems of a suboptimal CTF must still be resolved [6–8]. Digital refocusing has drawn considerable research interest because an optimal CTF can be maintained, which in principle prevents reductions in sensitivity and sidelobe issues [9–11]. A previously reported digital refocusing approach, called interferometric synthetic microscopy (ISAM), computationally reconstructs diffraction-limited transverse resolutions by solving the inverse scattering problem. However, the ISAM approach requires absolute phase stability during 3D image acquisition, which is difficult to realize *in vivo*, especially in endoscopic applications [9]. Recently, depth-encoded synthetic aperture, which we believe is a novel approach, has been reported. This approach extends the DOF by synthesizing different apertures and correcting the wavefront curvature caused by the defocus effect [10,11]. It does not require a phase-stabilizing setup, and it has low computational costs and good compatibility with conventional Fourier domain OCT (FD-OCT) hardware. However, an inherent issue of signal coupling loss caused by the mismatch between the NA of the fiber pinhole and apertures generated by the wavefront divider/splitter is observed, and an overall 50% signal loss can be attributed to the implementation of aperture division and the multiplexing

apparatus [10]. Here, we demonstrate a multiple aperture synthesis (MAS) technique to achieve a digital refocusing function without signal loss or sidelobe artifacts.

2. MULTIPLE APERTURE SYNTHESIS

The MAS technique extends the DOF in a spectral domain OCT (SD-OCT), which is analogous to synthetic aperture radar (SAR). In Figs. 1(a) and 1(a'), a microcylindrical lens (MCL) is positioned $\sim 10 \mu\text{m}$ away from the tip of the sample fiber with an axisymmetric configuration along the optical axis. All light paths of the spatial (angular) frequencies originating from the fiber pinhole are refracted sequentially by MCL, L1, and L2, and they intersect at the focal point of L2 with a uniform phase or optical path length. Under this ideal condition, a maximal constructive interference occurs at this focal point, which results in a diffraction-limited transverse point spread function (PSF). When the MCL is linearly shifted along a transverse direction perpendicular to the cylindrical axis by a piezoelectric transducer (PZT) [Figs. 1(b) and 1(b')], the spatial or angular frequency of the sample beam with respect to the full aperture of the focusing lens L2 is swept as the incidence angle at the curved surface of the MCL changes. The aberration caused by the cylindrical lens is not noticeable and the resolution in the x and y transverse dimensions is the same.

Figure 1(c) depicts the effective optical apertures in the objective lens (L2) pupil plane. Apertures 1–5 denote five apertures generated by transversely shifting the MCL. Figure 1(d) illustrates the spatial or angular frequency of focused beams 1–5, which correspond to apertures 1–5 in Fig. 1(c) in the focal plane of

the objective lens L2. During image acquisition, we chose to acquire an axial-line (A-line) at each of the five equally spaced spatial frequencies and synthesize five apertures together as shown in Fig. 1(e). Compared with the standard SD-OCT, more high spatial frequency light signals of the sample reflectivity can be coherently synthesized, which will theoretically and experimentally generate a larger aperture and an extended DOF.

The total optical path difference (OPD) between A-lines acquired in Figs. 1(a) and 1(b) is defined as $\Delta z = \Delta z_s + \Delta z_c$ and composed of two components: Δz_s , which is induced by the transverse shift of the MCL; and Δz_c , which is the defocusing term with $\Delta z_c = 0$ at the focus of L2. For a scatter located away from the focal point, when these OPDs are corrected to 0, the A-lines with distinctive apertures can be coherently summed together to form a digitally synthesized aperture.

In the classical theory of FD-OCT, the detected interference signal $I(k)$ in k -space includes a direct-current (DC) term, a cross-correlation (CC) term, and an auto-correlation (AC) term, and they are expressed in the following simplified formulation:

$$I(k) = S(k) \left[\text{DC} + 2 \int_{-\infty}^{\infty} \sqrt{I_r(k) I_s(k)} \cos(2kz) dz + \text{AC} \right], \quad (1)$$

where $S(k)$ is the spectral distribution of the light source and $I_r(k)$ and $I_s(k)$ are the electric field reflectivity from the reference arm and the sample arm, respectively, at depth z . Because only the CC encodes depth-resolved information for OCT imaging, $S(k)$, DC and AC can be omitted in the following derivation. The original CC term for the n th cross-sectional scan (B-scan) is

$$I_n(k) = \sqrt{I_r(k) I_s(k)} [\exp(i2kz_n) + \text{C.C.}], \quad (2)$$

where C.C. is the abbreviation for the complex conjugate, which will also be omitted in the following derivation. The subscript n represents the sequence number of distinctive apertures. To correct the OPDs and the defocus term, we define $k = k_0 + \Delta k$ and $z = z_n + \Delta z_n$, where z is the corrected optical path length for rendering a perfect focus. Then, Eq. (2) is rewritten as

$$I_n(k) = \exp(i\alpha_n) \cdot \sqrt{I_r(k) I_s(k)} [\exp(i2kz_n) \exp(i\beta_n)], \quad (3)$$

where $\alpha_n = -k_0 \cdot \Delta z_n$ and $\beta_n = -\Delta k \cdot \Delta z_n$. Equation (3) includes a constant phase α_n and an oscillation phase β_n , which are induced by multiple transverse shifts of the MCL and the defocusing term. The MAS process consists of two main steps to correct α_n and β_n in sequence.

First, according to the Fourier shift theorem, we correct the axial-delayed OPDs and axially shift them to the aligned depth by multiplying the B-scan by $\exp(-i\alpha_n)$. This step is called the axial shift. The n th axial-shifted B-scan is calculated as

$$I_n^{ax}(k) = I_n(k) \cdot \exp(-i\alpha_n), \quad (4)$$

where the superscript ax represents the axial-shift operation. When the criterion $|\sum_{n=1}^m I_n(k) \cdot \exp(-i\alpha_n)|$ reaches its maximum value, α_n achieves its optimal value α_n^{op} ; here, the superscript op represents the optimal value and m represents the total number of apertures.

Second, the constant phase β_n can be eliminated by multiplying the Fourier spectrum of Eq. (4) by a constant phase coefficient $\exp(-i\beta_n)$. This step is called the defocusing correction. The n th defocusing-corrected B-scan is calculated as

$$I_n^{\text{de}}(k) = I_n^{ax}(k) \cdot \exp(-i\beta_n), \quad (5)$$

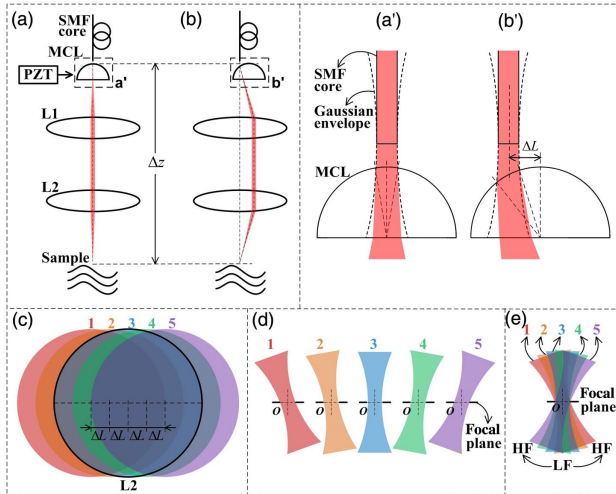


Fig. 1. Working principles of multiple aperture synthesis. (a) Schematic with a microcylindrical lens centered at the fiber pinhole. (b) Schematic with a microcylindrical lens (MCL) transversely shifted by a step size of ΔL . (a')–(b') Magnified views of the optical beam indicated by the dashed boxes in (a)–(b). (c) Five apertures generated by the transversely shifted microcylindrical lens and the aperture of the objective lens. (d) Focusing beams of the five apertures in (c). (e) Optical axes of the focusing beams of the five apertures in (c). SMF, single-mode fiber; MCL, microcylindrical lens; PZT, piezoelectric transducer; L1, collimating lens; L2, focusing lens; LF, low spatial frequency; and HF, high spatial frequency. Δz is the total optical path difference between A-lines acquired in (a) and (b), and composed of two components: Δz_s , induced by the transverse shift of the MCL and the defocusing term Δz_c . ΔL is the transverse shifting step size of the microcylindrical lens.

where the superscript de represents the defocusing-correction operation. To precisely correct the defocusing term, we must obtain the optimal β_n at depth z for each B-scan. The optimal $\beta_n(z)$ is strictly contained in the phase set $\{\pi/2, \pi, 3\pi/2, 2\pi\}$. When the criterion $\max\{|\sum_{n=1}^m I_n^{ax}(k) \cdot \exp[-i\beta_n(z)]|\}$ reaches its maximum value, $\beta_n(z)$ achieves its optimal value $\beta_n^{op}(z)$. Combining Eqs. (4) and (5), the digitally refocused B-scan is calculated as

$$I_{re} = \sum_{n=1}^m I_n(k) \cdot \exp[-i\alpha_n^{op}(z)] \cdot \exp[-i\beta_n^{op}(z)]. \quad (6)$$

This MAS achieves optimal constructive interference at the center of the scatter and destructive interference away from the center, which not only increases the total backscattered intensity but also preserves the diffraction-limited transverse resolution over a DOF extended multiple times.

3. NUMERICAL ANALYSIS

The image formation in an OCT system can be described by a CTF, which is the Fourier transform of the effective PSF [12–15]. Here, we define $p(m, n)$ as the pupil function (PF) of the objective lens. m and n are the corresponding radial spatial frequencies in two transverse directions. Because the light passes the objective lens twice, the 2D CTF can be obtained by convolving PFs of the illumination and detection aperture [15–18] as

$$C(m, n) = p(f\lambda m, f\lambda n) \otimes \otimes p(f\lambda m, f\lambda n), \quad (7)$$

where $\otimes \otimes$ represents the 2D convolution operation. f and λ represent the focal length of the objective lens and the wavelength of the illumination light. The PSFs are the Fourier transform of the CTFs in two transverse directions and are calculated as

$$F(x, y) = \int_{-\infty}^{\infty} \int_{-\infty}^{\infty} C(m, n) \exp[-2\pi i(mx + ny)] dm dn, \quad (8)$$

where x and y denote the variables on the plane perpendicular to the optical axis and z is the axial variable.

We performed numerical simulations using MATLAB software (MathWorks, Natick, Massachusetts, USA) to characterize the PFs, PSFs, and CTFs of the MAS technique with respect to available methods. Here, we consider three aperture types in the illumination and detection paths: full aperture, annular apodized aperture, and MAS. We define the radius of the full aperture as 1 [Fig. 2(a)] and the radii of the annularly apodized aperture as 0.7 [Fig. 2(b)]. In the case of MAS, five apertures were equally spaced with a transverse spacing of 0.25 as indicated by the bold numbers 1–5 in Fig. 2(c). Under the condition of Gaussian illumination, CTFs [Figs. 2(d)–2(f)] corresponding to PFs [shown in Figs. 2(a)–2(c)] were obtained by convolving PFs of the illumination and detection aperture. The 2D CTFs [Figs. 2(d)–2(f)] show that although the annular apodized aperture produces the largest frequency range, the cutoff spatial frequency of the MAS and full aperture is much greater than that of the apodization. The MAS technique has a better transverse CTF than the full aperture in the focal plane [Fig. 2(m)], and even has a similar transverse CTF as the full aperture at an out-of-focus plane of $z = b$ [Fig. 2(n)], where b is the confocal parameter. It is possible to obtain 2D PSFs [Figs. 2(j)–2(l)] via the Fourier transform of CTFs in two transverse directions. The apodized aperture produces the largest DOF but the worst sidelobes [−17.5 dB, Fig. 2(k)]. Both transverse PSFs of the full aperture [Fig. 2(j)] and MAS

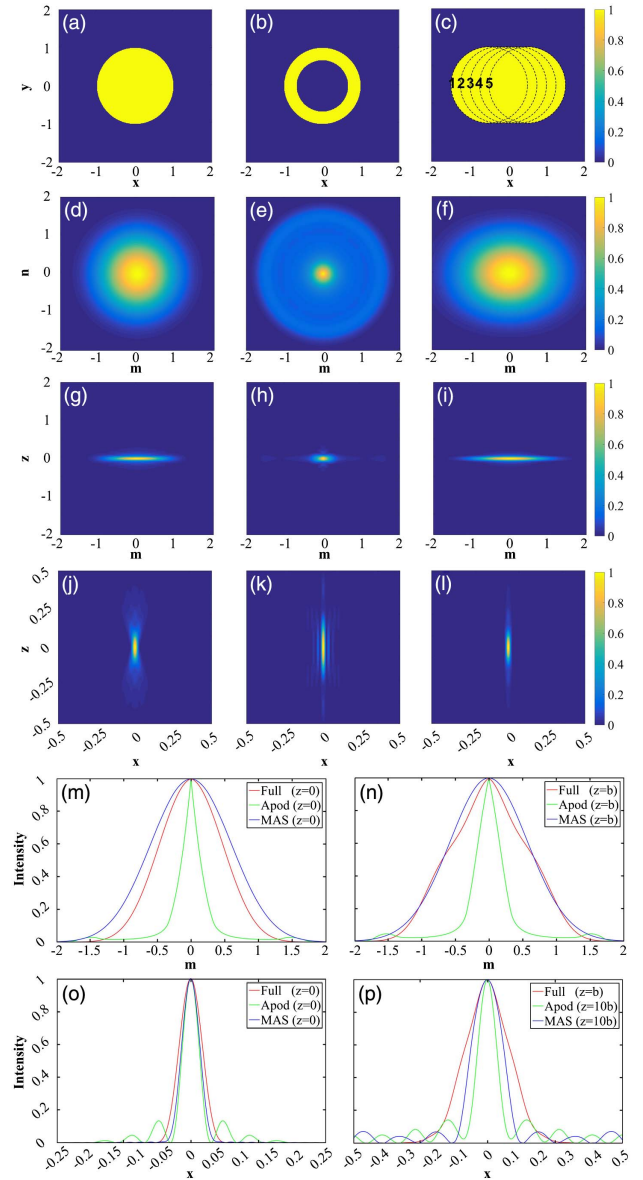


Fig. 2. Numerical simulation results. (a)–(c) PFs of a full aperture, an annular apodized aperture and an MAS. (d)–(f) Two-dimensional (2D) coherent transfer functions (CTFs) of a full aperture, an annular apodized aperture, and an MAS in the focal plane as a function over the transverse (m and n) spatial frequencies. (g)–(i) 2D CTFs of a full aperture, an annular apodized aperture, and an MAS as a function over the transverse spatial frequency (m) and axial (z) dimensions. (j)–(l) 2D PSFs of a full aperture, an apodization, and an MAS as a function over the transverse (x) and axial (z) dimensions. (m)–(p) Transverse CTFs in the focal plane and at an out-of-focus plane of $z = b$, respectively. b is the confocal parameter. (o)–(p) Transverse PSFs in the focal plane at an out-of-focus plane of $z = b$ and $10b$. Intensities in all figures are normalized by their maximum values.

[Fig. 2(l)] have insignificant sidelobes (<−61.9 dB and −46.4 dB, respectively), compared with the sidelobe of −20 dB in [8]. However, the DOF of the MAS [Fig. 2(l)] is much greater than that of the full aperture [Fig. 2(j)]. The FWHM transverse spot size of the full aperture doubles at depth b , whereas that of the apodized aperture and MAS are expanded by 13.9% and 73.0% [Fig. 2(p)] at depth $10b$, respectively. These results

indicate that the MAS technique can extend the DOF by a value that is more than 10 times that of the full aperture.

4. EXPERIMENTAL METHODS

A. Optical Coherence Tomography

The schematic of a MAS SD-OCT system is illustrated in Fig. 3. A superluminescent diode (SLD) array (T850-HP, Superlum, Carrigtwohill, Ireland) provides a broadband spectrum with an FWHM bandwidth of 165 nm centered at 850 nm. The light source, whose total output power is 18.0 mW, is split into a sample light and a reference light by a 2×2 wideband fiber-optic coupler (TW850R2A2, Thorlabs, Newton, New Jersey, USA) with a splitting ratio of 90:10. The light beam in the reference arm is collimated by lens L1 (AC050-010-B-ML, Thorlabs, Newton, New Jersey, USA), transmitted through a neutral density filter (NDL-10C-4, Thorlabs, Newton, New Jersey, USA) and focused by lens L2 (M Plan Apo NIR 20 \times , Mitutoyo, Takatsu-ku, Kawasaki, Japan) onto the reference mirror RM (PF10-03-P01, Thorlabs, Newton, New Jersey, USA). L2 and RM move together to match the path lengths in the sample and reference arms. The light beam in the sample arm is collimated by lens L3 (AC050-010-B-ML, Thorlabs, Newton, New Jersey, USA), projected onto the galvo scanner (GVS002, Thorlabs, Newton, New Jersey, USA), and then focused by the objective lens L4 (M Plan Apo NIR 20 \times , Mitutoyo, Takatsu-ku, Kawasaki, Japan). The mode field diameter (MFD) of the fiber (780 HP, Thorlabs, Newton, New Jersey, USA) is $5.0 \pm 0.5 \mu\text{m}$ (defined by the $1/e$ field) at 850 nm. The MCL is driven by a closed-loop PZT (AE0505D16F, Thorlabs, Newton, New Jersey, USA). A beam splitter (BS; BS017, Thorlabs, Newton, New Jersey, USA) is inserted in the sample arm to build up a dark-field apparatus. The backscattered light from the sample is focused by lens L5 (AC050-010-B-ML, Thorlabs, Newton, New Jersey, USA) and guided to the other 2×2 wideband fiber-optic coupler (TW850R2A2, Thorlabs, Newton, New Jersey, USA) with a splitting ratio of 90:10. The light beams from two arms are combined in the coupler and directed into the spectrometer after being collimated by the achromatic lens L6 (AC254-040-B-ML, Thorlabs, Newton, New Jersey, USA).

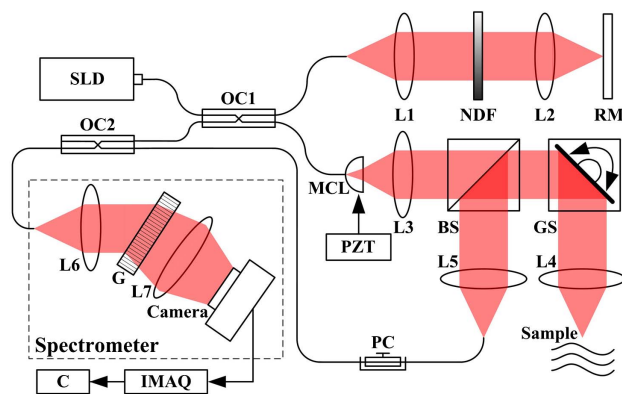


Fig. 3. Schematic of the MAS SD-OCT system. SLD, superluminescent diode; OC1-2, 90:10 fiber-optic coupler; L1, L3, L5, and L6, collimating lens; L2 and L4, focusing lens; L7, camera lens; NDF, neutral density filter; RM, reference mirror; MCL, microcylindrical lens; PZT, piezoelectric transducer; BS, beam splitter; GS, galvo scanner; G, transmission diffraction grating; IMAQ, image acquisition; C, computer; and PC, polarization controller.

The spectrometer consists of a 1765 line/mm diffraction grating (PING-Sample-020, Ibsen Photonics, Farum, Denmark), a camera lens (85 mm, $f/1.4$, Zeiss, Oberkochen, Germany) and a 4096-pixel charge-coupled device (CCD) camera (AViVA EM4, e2V, Chelmsford, UK). The detected spectrum is digitized at a 12-bit resolution and transferred to a computer via an image acquisition board (KBN-PCE-CL4-F, Bitflow, Woburn, Massachusetts, USA). Two-directional transverse scanning is implemented by two galvanometer-mounted mirrors driven with sawtooth pulses, which are generated by a 16-bit analog output of a data acquisition (DAQ) board (PCI-6221, National Instruments, Austin, Texas, USA). Image acquisition and galvo mirror scanning are synchronized by the external trigger from a DAQ digital output. A discrete Fourier transform is performed on each frame of the 1024 A-lines obtained by the CCD to resolve the axial depth profile of the sample.

B. Microcylindrical Lens Fabrication

We selected a closed-loop PZT with four embedded strain gauges and a travel range of $15.7 \mu\text{m}$. The output diverging beam of the sample fiber has a full angular range (defined by the $1/e^2$ power) of $7.45 (= 4\lambda/\pi\Delta x)$ deg, which is determined by the spot diameter Δx of the focused beam. The desired radius of the MCL is 60–70 μm , which is based on the travel range of the PZT and fiber NA. The MCL is precisely grinded from the coreless silica termination fiber (FG125LA, Thorlabs, Newton, New Jersey, USA). As shown in Fig. 4(a), the PZT is mounted on a two-axis goniometer (GNL20, Thorlabs, Newton, New Jersey, USA) and a three-axis compact stage (MBT616D, Thorlabs, Newton, New Jersey, USA). The inset provides a magnified view, which shows that two MCLs are cured on the silica. The cross-sectional width of the MCL is measured at 110 μm as shown in Fig. 4(b). Figure 4(c) is a side view showing the position of the MCL relative to the tip of the sample arm fiber.

C. Phantom Preparation

A phantom of polystyrene calibration microparticles was constructed by mixing agarose solution (No. PC0701-100 g, Vivantis, Oceanside, California, USA) with polystyrene microparticles (No. 64090-15, nominal size 6 μm , Sigma-Aldrich, St. Louis, Missouri, USA). This mixture was stored in a vial and

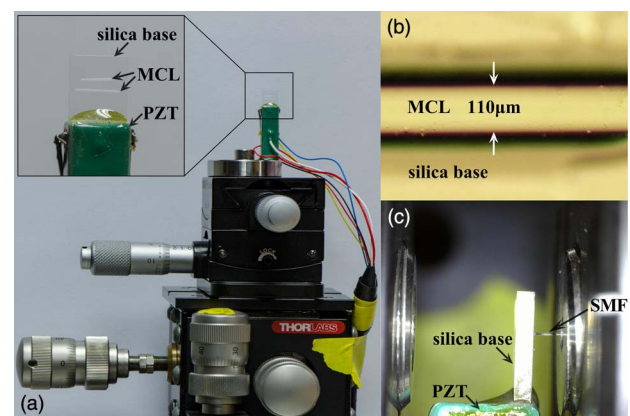


Fig. 4. PZT assembly and adjustment. (a) PZT is mounted on a two-axis goniometer stacked on a three-axis compact stage. Inset: Magnified view shows that two MCLs are cured on the silica base. (b) Cross-sectional width of the microcylindrical lens. (c) Alignment of the MCL and the tip of the sample fiber.

placed in an ultrasonic bath for 10 min to remove residual clusters. The sample (10 g) was poured into a cell culture dish, cured for 30 min at 100°C and then cured for 24 h at room temperature.

5. EXPERIMENTAL RESULTS

To demonstrate the performance of the DOF extension using the MAS technique, we conducted imaging experiments using the microparticle polystyrene calibration sample. Five B-scans ($m = 5$) were acquired using the MAS SD-OCT system, and they corresponded to five transverse shifts of the MCL with five distinctive apertures. One of B-scans was dispersion compensated using the algorithm in [19]. It is shown in Fig. 5(a), which indicates that the B-scans suffered from defocusing beyond the focus. According to Eqs. (4) and (5), the MAS process consisted of two steps: an axial shift and a defocusing correction. The results of the axial shift and defocusing correction are shown in Figs. 5(b) and 5(c), respectively. In Figs. 5(a')–5(c'), magnified views of two

calibration microparticles are indicated by the dashed boxes. We measured the transverse FWHMs of 50 microparticles at different depths in Figs. 5(a) and 5(c) and performed the 10-order polynomial-fitting as shown in Fig. 5(d). Because the MFD (defined by the $1/e$ field) was $5.0 \pm 0.5 \mu\text{m}$, the theoretical transverse FWHM of the PSF at focus was estimated at $2.92 \mu\text{m}$ and the corresponding DOF was $16.01 \mu\text{m}$ at the center wavelength of 850 nm. The finest transverse FWHM of the refocused microparticle was $9.06 \mu\text{m}$; thus, the finest nominal transverse FWHM of the PSF was 3.06 , which corresponded to a DOF of $17.30 \mu\text{m}$. The experimental results are consistent with the theoretical results. The DOF was estimated within a depth range from 910 to 927 μm , where two fitted lines crossed in Fig. 5(d). Over the full axial depth range of 1030 μm ($n = 1.33$), the maximum, averaged, and minimum transverse FWHMs of the microparticles in Fig. 5(a) were $39.34 \mu\text{m}$, $20.16 \mu\text{m}$, and $9.26 \mu\text{m}$, respectively; therefore, the maximum, averaged, and minimum transverse FWHMs of the PSFs were $33.34 \mu\text{m}$, $14.16 \mu\text{m}$, and $3.26 \mu\text{m}$, respectively. In contrast, the maximum, averaged, and minimum transverse FWHMs of the microparticles in Fig. 5(c) were $13.64 \mu\text{m}$, $11.21 \mu\text{m}$, and $9.06 \mu\text{m}$, respectively; therefore, the maximum, averaged, and minimum transverse PSFs were $7.64 \mu\text{m}$, $5.21 \mu\text{m}$, and $3.06 \mu\text{m}$, respectively. Thus, the MAS SD-OCT system appears to preserve the diffraction-limited transverse resolution over the full axial depth, and it obtained a DOF extension of ~ 10 -fold, which is consistent with the results of the numerical simulation in Section 3.

6. DISCUSSION AND CONCLUSIONS

We developed the MAS technique to address the fundamental problem of limited DOF in high transverse resolution FD-OCT. MAS is free from signal loss and sidelobe artifacts, which are caused by a suboptimal CTF function and inherent in the currently available methods. These merits of the MAS method have been demonstrated theoretically and experimentally in this work. Therefore, we believe the MAS technique has the potential to provide a sufficient DOF to stably acquire subcellular-resolution images *in vivo*. Moreover, the ability to manipulate the complex PF makes MAS a powerful tool that can eliminate various types of optical aberrations beyond the defocus induced by the sample or focusing optics, such as aberrations induced by human eye optics. However, the current study has two limitations. First, we used transverse priority scanning, which is susceptible to motion artifacts. This limitation can be easily resolved by changing to angular frequency priority scanning. Second, the current MAS form is implemented at the cost of scanning speed. In this work, we coherently sum five A-scans with five distinctive apertures together to obtain one DOF extended A-line, which decreases the imaging speed by five times. This limitation may be mitigated by the use of faster spectrometers or an ultra-high-speed swept source. Moreover, a phase ramp could be digitally created along the fast scanning direction in the PF to achieve digital transverse scanning. The proposed optical apparatus is applicable to desktop OCT imaging systems for DOF extension, but a significant research effort is required to develop a miniaturized optical design for endoscopic and intravascular applications. In conclusion, the proposed MAS technique overcomes the inherent tradeoff between DOF extension and signal loss/sidelobe artifacts and may ultimately overcome the DOF limitation in

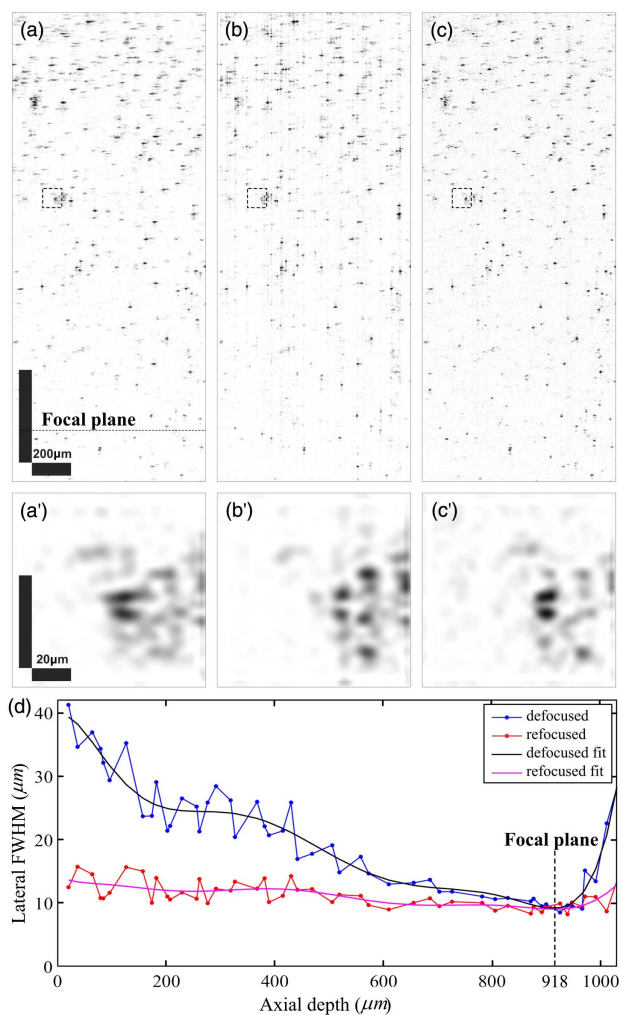


Fig. 5. Stepwise image sequence in linear scale: (a) Dispersion-compensated B-scan from one of five apertures; (b) Resulting B-scan of the axial-shift operation, which is the first step of the MAS; (c) Resulting B-scan of the defocusing correction operation, which is the second step of the MAS. (a')–(c') Magnified view of two calibration beads indicated by the dashed black boxes in (a)–(c). (d) Transverse FWHMs of 50 calibration beads at variable depths.

high-resolution OCT. Future works will focus on the development of a faster scanning MAS method for *in vivo* applications.

Funding. National Research Foundation Singapore (NRF) (NRF-CRP13-2014-05); Ministry of Education - Singapore (MOE) (MOE2013-T2-2-107); National Medical Research Council (NMRC) Singapore (NMRC/CBRG/0036/2013); Nanyang Technological University (NTU)-the Austrian Institute of Technology-the Medical University of Vienna (NTU-AIT-MUV) Program in Advanced Biomedical Imaging (NAM/15005).

REFERENCES

1. D. Huang, E. A. Swanson, C. P. Lin, J. S. Schuman, W. G. Stinson, W. Chang, M. R. Hee, T. Flotte, K. Gregory, and C. A. Puliafito, "Optical coherence tomography," *Science* **254**, 1178–1181 (1991).
2. D. Ferrara, K. J. Mohler, N. Waheed, M. Adhi, J. J. Liu, I. Grulkowski, M. F. Kraus, C. Baumal, J. Hornegger, and J. G. Fujimoto, "En face enhanced-depth swept-source optical coherence tomography features of chronic central serous chorioretinopathy," *Ophthalmology* **121**, 719–726 (2014).
3. H. G. Bezerra, M. A. Costa, G. Guagliumi, A. M. Rollins, and D. I. Simon, "Intracoronary optical coherence tomography: a comprehensive review: clinical and research applications," *JACC Cardiovasc Interv.* **2**, 1035–1046 (2009).
4. L. Liu, C. Liu, W. C. Howe, C. Sheppard, and N. Chen, "Binary-phase spatial filter for real-time swept-source optical coherence microscopy," *Opt. Lett.* **32**, 2375–2377 (2007).
5. L. Liu, J. A. Gardecki, S. K. Nadkarni, J. D. Toussaint, Y. Yagi, B. E. Bouma, and G. J. Tearney, "Imaging the subcellular structure of human coronary atherosclerosis using micro-optical coherence tomography," *Nat. Med.* **17**, 1010–1014 (2011).
6. K.-S. Lee and J. P. Rolland, "Bessel beam spectral-domain high-resolution optical coherence tomography with micro-optic axicon providing extended focusing range," *Opt. Lett.* **33**, 1696–1698 (2008).
7. Z. Ding, H. Ren, Y. Zhao, J. S. Nelson, and Z. Chen, "High-resolution optical coherence tomography over a large depth range with an axicon lens," *Opt. Lett.* **27**, 243–245 (2002).
8. R. Leitgeb, M. Villiger, A. Bachmann, L. Steinmann, and T. Lasser, "Extended focus depth for Fourier domain optical coherence microscopy," *Opt. Lett.* **31**, 2450–2452 (2006).
9. T. S. Ralston, D. L. Marks, P. S. Carney, and S. A. Boppart, "Interferometric synthetic aperture microscopy," *Nat. Phys.* **3**, 129–134 (2007).
10. J. Mo, M. de Groot, and J. F. de Boer, "Focus-extension by depth-encoded synthetic aperture in optical coherence tomography," *Opt. Express* **21**, 10048–10061 (2013).
11. E. Bo and L. Liu, "Spectral domain optical coherence tomography with extended depth-of-focus by aperture synthesis," *Proc. SPIE* **10024**, 1002451 (2016).
12. C. Sheppard and T. Wilson, "Depth of field in the scanning microscope," *Opt. Lett.* **3**, 115–117 (1978).
13. C. Sheppard and X. Mao, "Three-dimensional imaging in a microscope," *J. Opt. Soc. Am. A* **6**, 1260–1269 (1989).
14. M. Gu, X. Gan, and C. Sheppard, "Three-dimensional coherent transfer functions in fiber-optical confocal scanning microscopes," *J. Opt. Soc. Am. A* **8**, 1019–1025 (1991).
15. M. Gu and C. Sheppard, "Three-dimensional optical transfer function in a fiber-optical confocal fluorescence microscope using annular lenses," *J. Opt. Soc. Am. A* **9**, 1991–1999 (1992).
16. C. Sheppard, D. Hamilton, and I. Cox, "Optical microscopy with extended depth of field," *Proc. R. Soc. London Ser. A* **387**, 171–186 (1983).
17. M. Gu, C. Sheppard, and X. Gan, "Image formation in a fiber-optical confocal scanning microscope," *J. Opt. Soc. Am. A* **8**, 1755–1761 (1991).
18. M. Gu, *Principles of Three-Dimensional Imaging in Confocal Microscopes* (World Scientific, 1996).
19. X. Liu, S. Chen, D. Cui, X. Yu, and L. Liu, "Spectral estimation optical coherence tomography for axial super-resolution," *Opt. Express* **23**, 26521–26532 (2015).